

Investigation of Microphysical Processes Occurring in Isolated Convection during NAME

ANGELA K. ROWE, STEVEN A. RUTLEDGE, AND TIMOTHY J. LANG

Department of Atmospheric Science, Colorado State University, Fort Collins, Colorado

(Manuscript received 7 May 2010, in final form 9 September 2010)

ABSTRACT

To address questions regarding microphysical processes occurring in the core North American monsoon region, data from NCAR's S-band polarimetric Doppler radar (S-Pol) deployed during the North American Monsoon Experiment (NAME) in the summer of 2004, were used to investigate the location, size, and type of hydrometeors in convection. A cell identification and tracking algorithm was applied to this data over 100 h of microphysical scans, characterized by increased temporal and vertical resolution, to locate and track individual convective elements. Only isolated cells over land were included for this study to investigate potential elevation-dependent trends in microphysical processes in this region.

Examples of intense, isolated convection over all elevations revealed deep cells and polarimetric signatures comparable to other studies of tropical and midlatitude convection. A case over the low terrain highlighted deep, isolated convection with precipitation-sized ice extending to 15 km. In addition, the presence of differential reflectivity Z_{DR} columns in these cells indicated the lofting of supercooled water above the melting level, and an enhanced linear depolarization ratio L_{DR} "cap" above the column implied subsequent freezing to produce graupel. Similar features were also observed in an isolated cell over the western slopes, highlighting the combined roles of collision-coalescence and melting precipitation-sized ice for producing intense rainfall over the lower elevations. Despite previous observations of weaker and shallower cells with less precipitation ice over the Sierra Madre Occidental (SMO), case studies and general statistics using polarimetric data reveal the potential for accretional processes to also play an important role in producing intense rainfall over these higher elevations. For these isolated SMO cells, reduced warm-cloud depths, increased ice mass observed just above the melting level, and a narrower distribution of drop sizes suggest a reduced role of warm-rain processes compared to intense cells over the lower terrain. A potential relationship between microphysical processes and degree of organization is also hypothesized and will be the focus of a future study.

1. Introduction

The North American monsoon (NAM) develops in the Northern Hemisphere summer in response to changes in large-scale land-sea temperature contrasts (Higgins et al. 1997). Similar to its Asian counterpart, the onset of the NAM is characterized by a reversal in the mean low-level flow (Badan-Dangon et al. 1991) and marks an abrupt transition from hot, dry weather to relatively cooler, wetter conditions in the semiarid regions of southwestern United States and western Mexico (e.g., Douglas et al. 1993; Adams and Comrie 1997). Areas in northwestern Mexico receive 50%–80% of the annual water

through monsoon rainfall (Gochis et al. 2006), highlighting the need to accurately model and forecast precipitation within this core monsoon region. The predictability of warm-season rainfall in this region is limited by the lack of understanding of the nature of the precipitating systems, and is further complicated by the presence of steep topography (e.g., Adams and Comrie 1997; Berbery 2001; Gochis et al. 2002). A comprehensive network of instrumentation was deployed for the North American Monsoon Experiment (NAME) during the summer of 2004 to characterize and understand precipitation processes influenced by the complex terrain in northwestern Mexico (Higgins et al. 2006). The Sierra Madre Occidental (SMO), extending above 3 km, dominates the local topography of this core monsoon region and has been found to strongly influence the diurnal cycle of NAM precipitation (e.g., Gochis et al. 2004, 2007; Lang et al. 2007). Gochis et al. (2004), using data from the

Corresponding author address: Angela K. Rowe, Department of Atmospheric Science, Colorado State University, Fort Collins, CO 80523.

E-mail: arowe@atmos.colostate.edu

NAME Event Rain Gauge Network (NERN), described an elevation-dependent diurnal cycle in precipitation where rainfall occurs earliest and most frequently over the SMO, followed by a late evening/overnight peak across lower elevations with less frequency, but greater intensity. This diurnal trend has been mostly attributed to a westward propagation of systems off the SMO and upscale growth into mesoscale convective systems (MCSs) over the coastal plain (Lang et al. 2007).

In addition to the diurnal variability of precipitation, the vertical structure and microphysical characteristics of convection require investigation to improve the understanding and prediction of warm-season rainfall in the NAM region. In particular, knowledge of the microphysical structure is crucial for accurate estimates of precipitation from remote sensing observations (e.g., Nesbitt et al. 2008). In addition, hydrometeor identification allows for microphysical and convective parameterizations to be validated and improved, which significantly affect the model-simulated regional climate during the NAM (e.g., Gochis et al. 2002). Previous studies from NAME have shown that convection over the high terrain of the SMO tends to be shallower than convection over the foothills and lower terrain (e.g., Nesbitt et al. 2008; Rowe et al. 2008). Analyses of heat sources, heating rates, and moisture sources/sinks over the SMO also indicate shallow convection over the high terrain during the early afternoon hours (Johnson et al. 2010), consistent with radar and satellite observations. In addition to taller echo tops, Rowe et al. (2008) illustrated that convection over the coastal plain was characterized by greater warm-cloud depths, defined as the distance between the lifting condensation level and the melting level, located at an average height of 5 km, and therefore a deeper layer over which accretional growth could occur. Rowe et al. (2008) suggested that the elevation-dependent trends in rainfall intensity may be explained by the observed differences in warm-cloud depth between the SMO and coastal plain. In addition, vertically intense cells containing large ice particles (i.e., graupel and small hail) have been observed in the NAME domain (Higgins et al. 2006), suggesting a contribution of cold cloud processes to rainfall production. Therefore, a major remaining objective of NAME (and the basis of this study) is to determine microphysical processes, including the relative roles of warm-rain and ice-based particle growth, as a function of topography.

A recent study by Lang et al. (2010), using radar data from NAME, further suggested an increase in intensity of all convective features in the domain with decreasing elevation. Their analyses revealed an increase in ice and water masses associated with convection over the lower terrain, as well as larger rain drops compared to over the

SMO. These results further indicate differences in microphysical processes as a function of elevation, where shallower warm-cloud depths and liquid water mass imply a lesser role of warm-rain processes in convection over the higher terrain, yet an increased ice mass over the coastal plain suggests an important contribution from ice-based processes in enhancing rainfall intensity.

To address remaining questions about the microphysical processes occurring in this region, this study used data from the National Center for Atmospheric Research (NCAR) S-band polarimetric Doppler radar (S-Pol) to provide information regarding the distribution and evolution of hydrometeor types in NAME convection that could be detected by S-Pol. Compared to previous NAME studies that included all precipitating features, this analysis focuses on unorganized convection to evaluate the vertical structure and temporal evolution of individual convective elements through a case study approach. A follow-on study will examine the characteristics of organized (mesoscale) convection in this core monsoon region. Section 2 of this paper describes the cell tracking algorithm and feature analysis used to identify isolated convection. Examples of convective cells spanning a range of topography will be presented in section 3 to investigate the distribution and evolution of hydrometeors within isolated cells. Cell characteristics inferred from these case studies will be placed within the greater context of unorganized convection in section 4 through a more general analysis using polarimetric radar data. Last, overall conclusions will be discussed in section 5.

2. Data and methodology

a. S-Pol data

During the 2004 NAME field campaign, the NCAR S-Pol radar was located along the Gulf of California coast about 90 km north of Mazatlan, Mexico, providing nearly continuous data from 8 July through 21 August (Higgins et al. 2006; Lang et al. 2007). Full-volume, 360° scans every 15 min at elevation angles of 0.8°, 1.3°, and 1.8° allowed for echo detection and rain-rate estimation out to a range of 210 km. A less common sector-scanning mode focused on specific precipitation features, with sector widths between 90° and 120° and elevation angles selected based on the proximity of the features to the radar, to provide increased temporal (and spatial) resolution of 6–7 min for 36 cases at a maximum range of 150 km. In some cases, RHIs were included to complete the total 15-min scanning pattern, providing fine-scale vertical resolution of convection. As a result of this improved temporal information, radar volumes used in

this study were selected from these microphysical cases, composing about 95 h of total scanning time. It is necessary to note that these approximate 100 h of scanning time were likely focusing on interesting, intense cases, and neglected the weaker convection, especially over the SMO. For this reason, cases presented in this study represent more intense examples of convection compared to previous NAME studies.

Extensive quality control of the raw S-Pol data, discussed in detail in other NAME publications (Lang et al. 2007, 2009), involved calibration of the power-based variables, removal of nonmeteorological and second-trip echo, attenuation correction, and correction for partial beam blockage. Accuracy of reflectivity was ± 1 dBZ except in blocked regions. Differential phase ϕ_{DP} was filtered, based on a technique described by Hubbert and Bringi (1995), in order to calculate specific differential phase K_{DP} used for rainfall analyses and hydrometeor identification. The suite of radar variables used in this study included horizontal reflectivity Z_H , differential reflectivity Z_{DR} , providing information about oblateness of the hydrometeors, linear depolarization ratio L_{DR} , and the zero-lag cross-correlation coefficient $\rho_{HV}(0)$, which both aid in distinguishing between pure rain and mixtures of hydrometeors, and K_{DP} . A more complete description of the polarimetric variables and their application to microphysical studies can be found in Bringi and Chandrasekar (2001). The corrected radar data was then gridded to Cartesian coordinates at a 1-km horizontal and 0.5-km vertical resolution using the program REORDER (Mohr et al. 1986). Finally, using the gridded polarimetric variables [Z_H , Z_{DR} , K_{DP} , L_{DR} , $\rho_{HV}(0)$] and a mean temperature profile from Mazatlan during the field experiment, a hydrometeor classification algorithm, based on the methodology of Liu and Chandrasekar (2000) and described in detail by Tessendorf et al. (2005), was applied to determine the dominant hydrometeor type at each horizontal and vertical grid point.

b. Cell identification and tracking

To objectively identify convection during NAME, a tracking algorithm, similar to that described by Gauthier et al. (2010), was applied to the gridded S-Pol radar data. This variation of the Thunderstorm Identification, Tracking, Analysis, and Nowcasting (TITAN) program (Dixon and Wiener 1993) was used to locate and track individual cells throughout the S-Pol domain over the time period for each case. This technique, referred to as the centroid identification and tracking scheme, has been applied in previous studies to develop nowcasting algorithms using radar data (e.g., Crane 1979; Rosenfeld 1987; Dixon and Wiener 1993; Johnson et al. 1998). The

strength of this method over others (e.g., cross-correlation tracking; Rinehart and Garvey 1978; Li et al. 1995) is its effectiveness in tracking individual, isolated storms, allowing for temporal evolution of cell characteristics to be investigated (Johnson et al. 1998).

Prior to identifying cells, a composite reflectivity field was created by determining the maximum reflectivity within the vertical column at each grid point. At each time step, regions with composite reflectivity greater than 35 or 45 dBZ were defined as potential cells, and a unique index number was assigned to each of these cells. Although absent in the single-threshold TITAN algorithm presented by Dixon and Wiener (1993) and the tracking methodology used by Gauthier et al. (2010), the use of these multiple reflectivity thresholds has been implemented in the Storm Cell Identification and Tracking (SCIT) algorithm (Johnson et al. 1998), where it has been shown to improve identification of intense, embedded cells. The choice of using the specific thresholds of 35 and 45 dBZ was somewhat arbitrary; however, these values set a reasonable limit for convection (e.g., DeMott and Rutledge 1998), thereby restricting the identification to convective-only elements. Sensitivity tests of these values have shown that lowering the threshold reduces the intensity and increases the size of the cells, with a greater number of apparent cell mergers (e.g., Dixon and Wiener 1993; Gauthier et al. 2010). For this analysis, isolated cells were compared based on terrain elevation as opposed to convective versus stratiform elements; therefore, the sensitivity of the reflectivity thresholds did not impact the results of this study.

A minimum area threshold was also implemented to prevent tracking of any noise or clutter remaining in the gridded data. For this study, a two-pixel minimum (i.e., 2 km^2) was required for cells identified by the 45-dBZ threshold, and, similar to the area threshold used in SCIT (Johnson et al. 1998), potential cells with reflectivity greater than 35 dBZ had to contain at least 10 grid points, corresponding to an area of 10 km^2 . This differs slightly from the 8-km^2 threshold imposed by Gauthier et al. (2010), but both act to eliminate noisy pixels. For cells that met the reflectivity and area criteria, an ellipse-fitting method, described by Nesbitt et al. (2006), was used to estimate the major and minor dimensions of the identified cell. To focus this study on unorganized, isolated convection, a feature identification scheme was then applied to the cells. The identification of precipitating features during NAME is described in detail by Lang et al. (2007), and the classification of feature types, based on a scheme described by Rickenbach and Rutledge (1998), is explained by Pereira (2008) for this dataset. Specifically, if the major axis of the cell's fitted ellipse did not exceed 100 km, and if

the aspect ratio between the major and minor axes of the convective areas was less than 5 to 1 (Bluestein and Jain 1985), then the cell was considered sub-MCS, non-linear; these cells will be referred to as isolated convection in this study. This differs from previous NAME radar studies (e.g., Lang et al. 2007, 2010; Rowe et al. 2008) where convective partitioning was applied to reflectivity grids regardless of size or degree of organization. A later study will compare these observations of isolated convection to convective cells that exhibit mesoscale organization.

Initially all individual cells in the volume scan were assigned unique track numbers, and the cell's position was recorded as the location of the reflectivity-weighted centroid. For the next radar volume, this initial location was used as the projected position of the track to be compared to the cell locations in the new volume. The distance between the projected center of the track and the center of the new cell was computed in both east-west and north-south directions, after which the angle between these distances was used to convert the projected path to Cartesian coordinates. Finally, using the axis information from the initial ellipse, the projected ellipse was determined for the track. Similarly, this method tested whether the new cell's ellipse contained the projected center of the track. The mean movement of the track was then added to the previous reflectivity-weighted centroid at each subsequent time step to relate new cells to previously defined tracks. If more than one possible track was identified for a given cell, a merger of cells was noted, and the cell with the peak reflectivity dominated the cell in the merger. An example of this can be seen in Fig. 1, where a merger is evident between cells 144 and 146 at time 2209 UTC to form cell 158 at time 2217 UTC. In this case, cell 158 would be considered part of the same track as cell 144 (the cell with higher reflectivity), and the track associated with cell 146 would be terminated. Also, if several new cells were associated with an existing track, this scenario was classified as a split. Any new cells that did not correspond to a previous track were given a new track number such that all cells in a volume were associated with a specific track. This method created some complications for evaluating a cell's lifetime, as it needed to be determined if the initial (final) point of a cell's track was representative of the growing (decaying) stage of the cell or if it resulted from a split (merger); however, especially for the case studies presented in this study, it proved useful for studying the evolution of individual convective cells.

c. Cell properties

Each grid point contained within the tracked cells was matched with the gridded polarimetric data at that

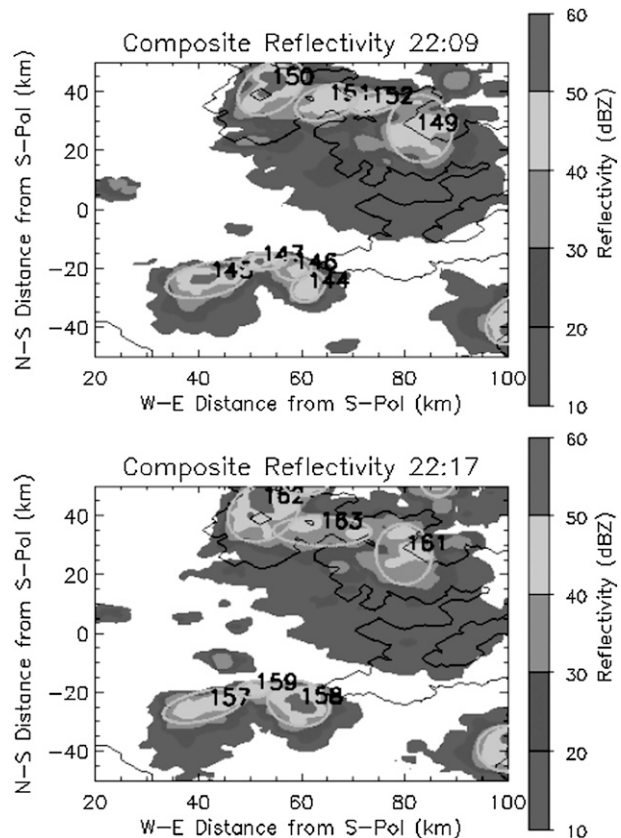


FIG. 1. Gridded composite reflectivity (filled contours) for (top) 2209 and (bottom) 2217 UTC 10 Jul 2004. Tracking ellipses are shown in gray and associated cell numbers are identified by the bold, black numbers. Overlaid in black contours is the topography at 0, 1, 2, and 3 km.

location, and vertical cross sections of polarimetric variables were created through isolated cells to investigate their vertical characteristics. Echo-top heights were estimated by the height of the 0-dBZ reflectivity contour in each individually tracked cell. To aid in the microphysical analyses, ice and liquid water masses were also calculated for each cell based on the methodology described by Carey and Rutledge (2000) and Cifelli et al. (2002). Using a modified version of the Colorado State University blended polarimetric algorithm (Cifelli et al. 2002), near-surface rainfall rates were computed for each cell location. Polarimetric-based equations for estimating rainfall, tailored to the NAME region, were applied to this radar dataset in a similar manner as previous studies (e.g., Lang et al. 2007; Rowe et al. 2008). Applying this algorithm to all grid points within a cell allowed for mean and maximum rainfall rates to be calculated for each convective element. By relating these rainfall rates to hydrometeor characteristics within the cell, details about the microphysical processes occurring in this region could be described, as

well as the specification of elevation-dependent trends and changes that occurred as the precipitating features evolved.

d. Topographic data

Topographic data was obtained from the National Geophysical Data Center (NGDC), available on a 0.02° grid, and was matched to the radar grids, as described in Lang et al. (2007). Maximum terrain height was determined within a 2-km area surrounding a particular grid point. This information was divided into four elevation groups: 0–1 km, 1–2 km, greater than 2 km, and water in order to remain consistent with NAME precipitation studies by Gochis et al. (2004) and Rowe et al. (2008). Our radar analysis is organized over these four elevation groupings.

3. Results

a. Case studies

To evaluate the relative roles of warm-rain and ice-based precipitation production, a case study approach was used to locate and describe the evolution of hydrometeors within isolated cells. Analysis of a cell in this manner required its entire life cycle to be captured by S-Pol, and cases were chosen over a range of topography. Although previous studies have noted differences in convection occurring over the water compared to that over land (i.e., Lang et al. 2010), this study will neglect cells over the Gulf of California because the frequency of occurrence of isolated convection over water was low (Fig. 2); the majority of these cells were associated with organized systems moving off the coast during the early morning hours. The following subsections will describe a number of cases selected from the upper 25th percentile of tracks, in terms of echo-top height, reflectivity, and maximum rainfall rate, within each elevation group to compare and contrast intense convection over a range of topography. Median values of properties from all tracked isolated cells are presented in Table 1 to provide a basis for comparison for the following cases.

1) COASTAL PLAIN

An intense example of isolated convection over low terrain (0–1 km) occurred on 10 July 2004. On this day, upper-level (200 hPa) northerly flow overlaid low-level (850 hPa) southwesterly flow in an environment with approximately 2000 J kg^{-1} of CAPE. The lack of any large-scale synoptic features influencing the area allowed for diurnally forced convection to dominate the precipitation totals, with convective initiation focused over the SMO during the afternoon. Additional convection

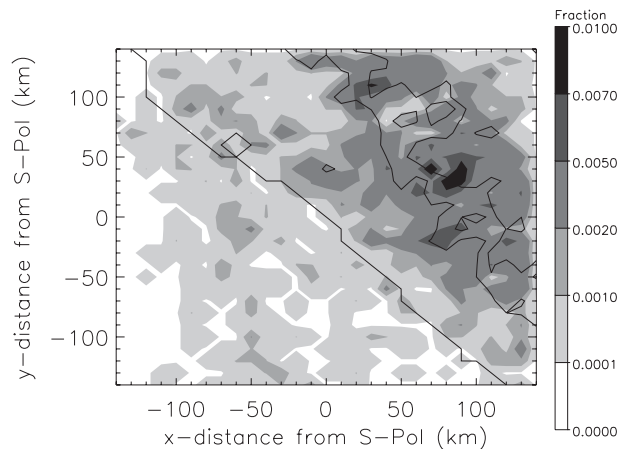


FIG. 2. Frequency of occurrence of isolated cells (shaded contours) at each grid location, where frequencies are normalized by the total number of isolated cells in the domain. Bold, black contours represent the topography contoured at 0, 1, 2, and 3 km.

formed over the lower terrain around 2130 UTC, with the cell of interest developing over a slightly elevated area on the coastal plain due to diurnal heating. The maximum rainfall rate for this cell was 81 mm h^{-1} compared to a median maximum rate of 36 mm h^{-1} for isolated cells over the low terrain (Table 1). Peak reflectivity of 59 dBZ exceeded the median value by 12 dBZ, and echo-top heights were also above average, although the radar did not top this cell because of its proximity to the radar (approximately 50 km).

An RHI from 2159 UTC (Fig. 3) provides a detailed view of the vertical structure and hydrometeor characteristics of this intense, isolated cell through analysis of the polarimetric data. This image highlights a mature cell with a deep, narrow reflectivity core of 50 dBZ reaching 10 km and a narrow column of $Z_{DR} > 1.5 \text{ dB}$ extending 1–2 km above the melting level height of 5 km, commonly referred to as a positive Z_{DR} column. Such Z_{DR} columns imply the presence of supercooled raindrops lofted by strong updrafts (e.g., Illingworth et al. 1987), and have also been observed in numerous studies of convection including hail-producing, U.S. high plains storms (e.g., Bringi et al. 1996; Tessendorf et al. 2005), isolated cells in Florida (e.g., Jameson et al. 1996; Bringi et al. 1997) and Alabama (Fulton and Heymsfield 1991), intense convection over the Tiwi Islands (e.g., Carey and Rutledge 2000; Keenan et al. 2000), and convection in Amazonia (e.g., Cifelli et al. 2002). Typically, a region of enhanced L_{DR} , known as an L_{DR} “cap,” is observed above the Z_{DR} column because of the rapid freezing of supercooled drops and subsequent acquisition of a water-coat due to collisions with liquid drops (e.g., Bringi et al. 1996). Jameson (1983)

TABLE 1. Median values of specific variables for all isolated cells in a particular elev group.

| Elev subset | No. of unique tracks | Median max rain rate (mm h ⁻¹) | Median lifetime (min) | Median water mass (g m ⁻³) | Median ice mass (g m ⁻³) | Median max Z (dBZ) | Median echo-top height (km) |
|-------------|----------------------|--|-----------------------|--|--------------------------------------|--------------------|-----------------------------|
| 0–1 km | 488 | 35.7 | 29 | 0.33 | 0.05 | 47 | 12.5 |
| 1–2 km | 366 | 32.2 | 30 | 0.30 | 0.06 | 45.5 | 13 |
| >2 km | 377 | 32.4 | 29 | 0.27 | 0.10 | 44 | 12.5 |

noted the presence of the L_{DR} cap atop positive Z_{DR} columns in the inflow side of a cell, indicating the process in which raindrops within the column likely grew initially via the collision-coalescence process. As updrafts increase, supercooled drops are lofted above the melting level into colder environments, allowing the drops to freeze and serve as embryos for rapid accretional growth. This process can be inferred from Fig. 3

with L_{DR} values increasing to -16 dB above the Z_{DR} column, likely due to the existence of wetted, aspherical ice particles (e.g., graupel). Values of $\rho_{HV}(0)$ are lower in this region compared to the surrounding areas (0.9–0.92), further indicating the coexistence of liquid and frozen drops and a dispersion of particle shapes.

A series of vertical cross sections through this cell (Figs. 4a–d) from 2146 through 2209 UTC places the

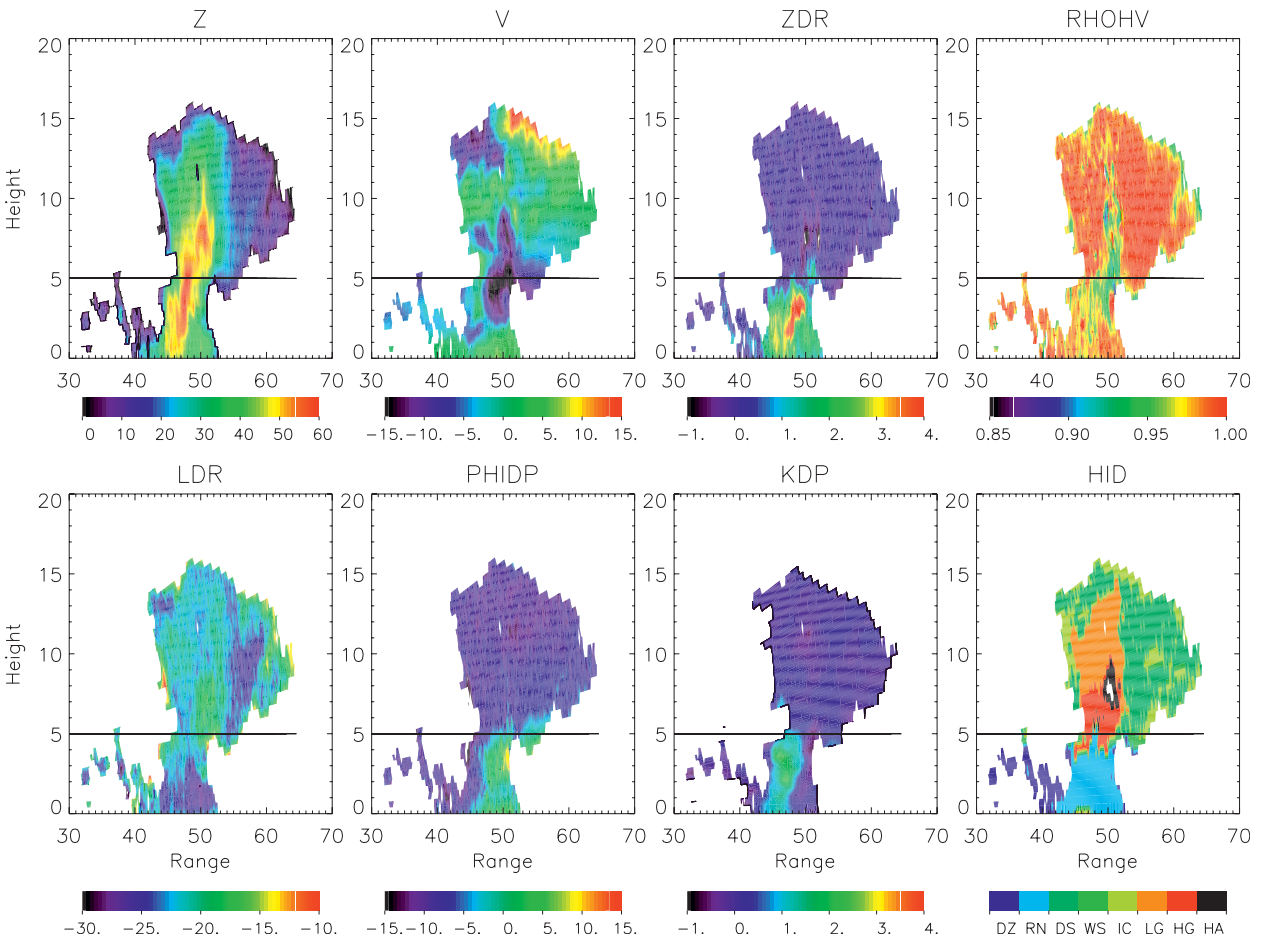


FIG. 3. RHI through an isolated cell at 2159 UTC 10 Jul 2004 at a 118° azimuth angle. Variables from left to right, starting with the (top), include reflectivity Z (dBZ), radial velocity V_R (m s⁻¹), differential reflectivity Z_{DR} (dB), correlation coefficient ρ_{HV} , linear depolarization ratio L_{DR} (dB), differential phase Φ_{DP} (°), specific differential phase K_{DP} (° km⁻¹), and the HID. HID abbreviations correspond to the following: drizzle (DZ), rain (RN), dry snow (DS), wet snow (WS), ice (IC), low-density graupel (LG), high-density graupel (HG), and hail (HA). The solid black line at 5 km indicates the location of the melting level. Height is in km, and range is distance in km from S-Pol.

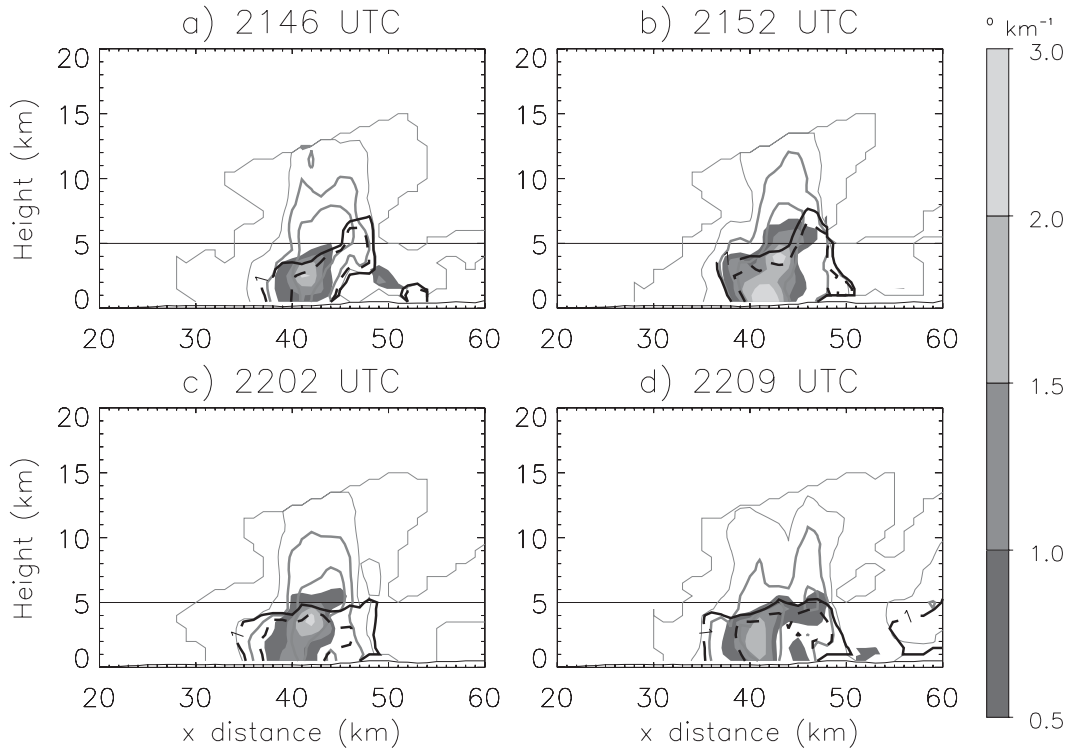


FIG. 4. Vertical cross section through the cell occurring on 10 Jul 2004 at the point of maximum reflectivity at (a) 2146, (b) 2152, (c) 2202, and (d) 2209 UTC. The x axis represents the distance from S-Pol in km. Filled contours show K_{DP} in $^{\circ} \text{km}^{-1}$. Gray contours show reflectivity at 0, 30, 40, and 50 dBZ, where the 40- and 50-dBZ contours are thickened. Values of Z_{DR} are contoured in black for 1 (solid) and 2 dB (dashed). Terrain height is plotted at the bottom as a black contour. The solid black line at 5 km represents the average height of the melting level during this cell's lifetime.

previously described RHI in the context of the cell evolution. The initial occurrence of the Z_{DR} column (Fig. 4a) coincided with the presence of the L_{DR} cap (Fig. 5a), indicating the lofting of raindrops above the

melting level and production of graupel and small hail. Subsequent melting of these large ice hydrometeors can be inferred from the local maximum in K_{DP} , with values exceeding 2°km^{-1} below the melting level (Fig. 4a).

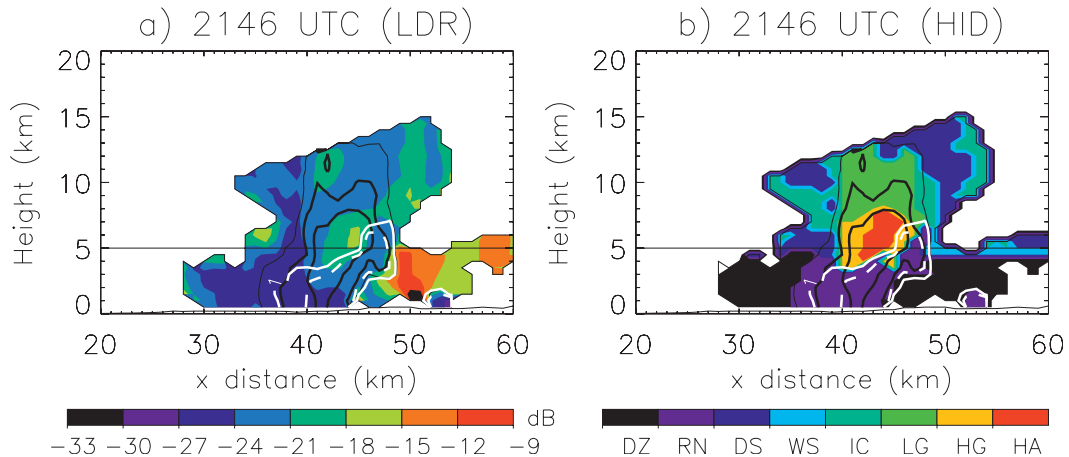


FIG. 5. Color-filled contours represent (a) L_{DR} (dB) and (b) HID. The HID abbreviations are the same as described in Fig. 3. Black contours show reflectivity at 0, 30, 40, and 50 dBZ, where the 40- and 50-dBZ contours are thickened. Values of Z_{DR} are contoured in white for 1 (solid) and 2 dB (dashed). Terrain and melting level height are as in Fig. 4.

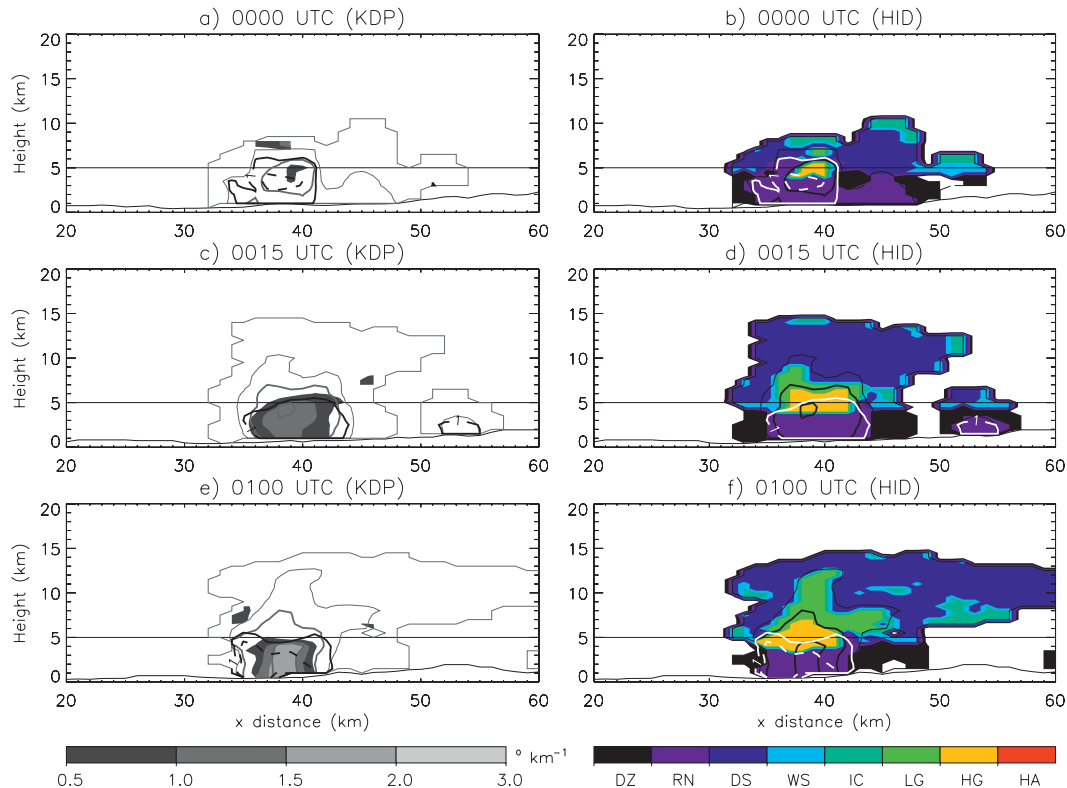


FIG. 6. Vertical cross sections through the maximum reflectivity of a cell at (a),(b) 0000; (c),(d) 0015; and (e),(f) 0100 UTC 19 Aug 2004. (left) K_{DP} ($^{\circ} \text{km}^{-1}$) as described in Fig. 4 and (right) HID as described in Fig. 5.

Indeed, the Hydrometeor Identification (HID) algorithm identified a large region of hail at this time (Fig. 5b), further suggesting the riming processes implied from the Z_{DR} and L_{DR} fields. This, however, was short-lived as the large ice hydrometeors rapidly fell out, melted, and continued to produce enhanced K_{DP} below the melting level at 2152 and 2202 UTC (Figs. 4b,c). At 2202 UTC, the Z_{DR} column was no longer present, suggesting a weakening of the updraft, and by 2209 UTC (Fig. 4d), the core had descended with maximum K_{DP} near the surface, marking the decaying stage of the cell.

This particular example showed that in addition to coalescence, mixed-phase processes played a role in rainfall production in this intense convective cell via drop freezing and subsequent riming growth, similar to processes described in tropical cumulonimbi (e.g., Takahashi 1990; Takahashi and Kuhara 1993). Similar results were also presented from the Tropical Rainfall Measuring Mission Large-Scale Biosphere–Atmosphere (TRMM-LBA) experiment in Amazonia, where lofting of supercooled rainwater into the mixed-phase zone and the resulting production of large amounts of precipitation ice via drop freezing were observed in convection occurring during the easterly regime (Cifelli et al. 2002). In addition, this process was noted during the Maritime

Continent Thunderstorm Experiment (MCTEX) over the Tiwi Islands where analysis of a lightning-producing cell showed the freezing of supercooled raindrops as an important source of precipitation-sized ice in tropical convection (Carey and Rutledge 2000).

2) WESTERN SLOPES

Over the western slopes of the SMO (1–2 km), where rainfall rates tended to be maximized relative to the other terrain elevations, the vertical structure of intense, isolated convection was similar to cells over the coastal plain. One example, representing an intense cell in this elevation group, developed and persisted over the western slopes about 60 km to the northeast of S-Pol during the evening of 18 August 2004. Maximum rainfall rates for this cell exceeded 100 mm h^{-1} , compared to the median maximum rate over the western slopes of 33 mm h^{-1} . Echo tops reached 15.5 km, compared to a median of 13 km, and the peak reflectivity of 53 dBZ exceeded the median by 7 dBZ. At 0000 UTC 19 August, a vertical cross section through this feature (Fig. 6a) shows a relatively shallow cell with weak reflectivity and low K_{DP} ($0.5^{\circ} \text{km}^{-1}$). The HID at this time (Fig. 6b) identified graupel; however, these hydrometeors were limited to below 7 km during this early stage of development.

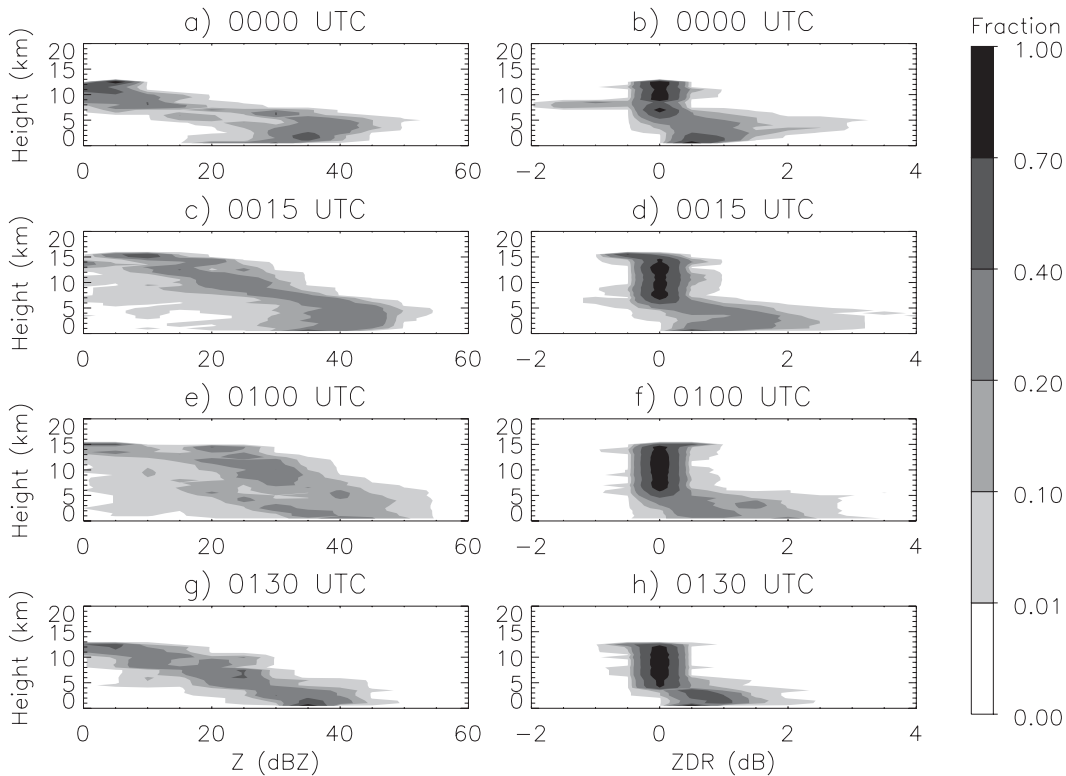


FIG. 7. CFADs of (left) Z and (right) Z_{DR} associated with the cell at 0000, 0015, 0100, and 0130 UTC 19 Aug 2004. Frequencies are normalized by the total frequency in each height bin.

Fifteen minutes later, the radar echo top of the cell reached 15 km (Fig. 6c) with graupel up to 11 km (Fig. 6d). This rapid growth, coincident with the increasing abundance of graupel, suggests a rapid glaciation process, where the rise in echo top results from the release of the latent heat of fusion (e.g., Cotton and Anthes 1989).

An RHI was not available for this cell; therefore, the use of contoured frequency by altitude diagrams (CFADs) of reflectivity and differential reflectivity was employed to provide an additional method for evaluating microphysical processes (Yuter and Houze 1995). In particular, the key feature of the reflectivity CFAD involves the onset of diagonalization of the mode of the joint frequency distribution of reflectivity with height, which indicates the fallout of large hydrometeors and termination of accretional growth processes; in addition, the slope of the Z_{DR} CFAD reveals information about the corresponding drop sizes. Figure 7 shows CFADs of Z (left) and Z_{DR} (right) for the previously described example over a selection of times throughout the cell's evolution. The abrupt vertical growth of the cell between 0000 and 0015 UTC is also seen in these plots (Figs. 7a,c), with reflectivities of 30 dBZ reaching 14 km at the latter time. In the lower levels, the mode of reflectivity shifts from 35 to 45 dBZ during this 15-min

interval, with a local maximum in frequency just beneath the melting level at 0015 UTC characteristic of melting ice hydrometeors. This corresponds to the elevated maxima in reflectivity and K_{DP} greater than $1^{\circ} \text{ km}^{-1}$ seen in the vertical cross section (Fig. 6b), indicating the melting of graupel following the rapid glaciation of the system. In addition, the occurrence of negative Z_{DR} at 0000 UTC above the melting level indicates the presence of large ice hydrometeors, which are likely forming due to the freezing of drops and subsequent riming. This coincides with the rapid growth of the cell due to glaciation, as previously described, and the shift in the peak and range of Z_{DR} values in the low levels from 0000 (Fig. 7b) to 0015 UTC (Fig. 7d) emphasizes the contribution to rainfall of melting ice.

By 0100 UTC, the reflectivity core and largest K_{DP} values had lowered to near the cloud base (Fig. 6e), coincident with the peak rainfall rate of 100 mm h^{-1} . The reflectivity CFAD at this time (Fig. 7e) shows a broader range of low-level reflectivity values, extending from 0 to 55 dBZ, further indicating a descending core. Similar to the reflectivity CFAD analysis of Yuter and Houze (1995), this shift in the distribution indicates the mature stage of the cell, where fewer new particles were being injected into the upper levels of the cell and

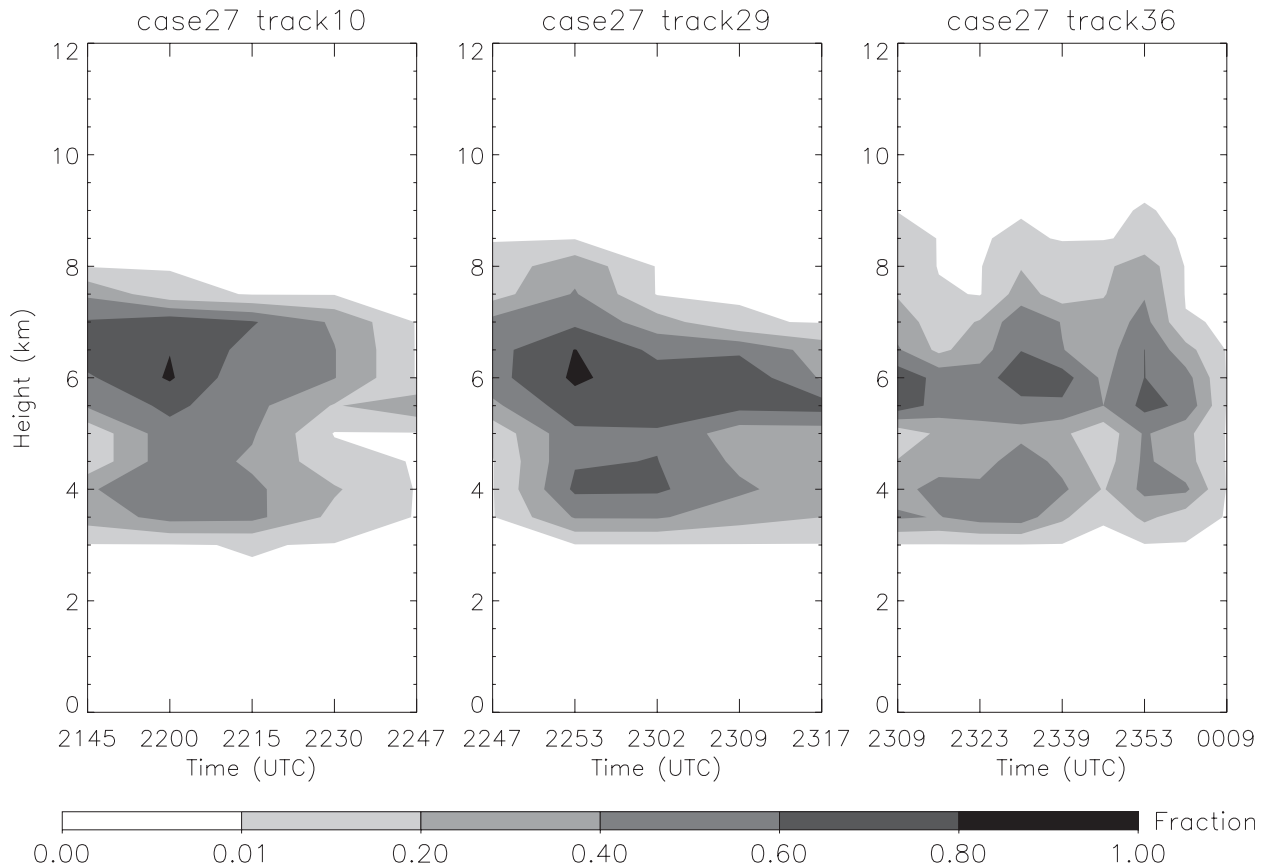


FIG. 8. Contours show the fraction of grid points at a particular height where the HID was identified as graupel for three isolated cells over the SMO on 14 Aug 2004.

the large, more reflective ice particles were falling out and melting. This also corresponds to a wide range of Z_{DR} values below the melting level (Fig. 7f), which suggests contributions from both large and small drops to the rainwater mass. At 0130 UTC, the final time of the cell's track, increased diagonalization is apparent in the reflectivity CFAD (Fig. 7g), indicating the demise of dominant accretional growth and suggesting a weakening of the main updraft (e.g., Zeng et al. 2001). In addition, the peak in frequency of Z_{DR} (Fig. 7h) at low levels shifts to lower values, signifying a reduced contribution from large, melting hydrometeors to the rainfall and likely the break up of larger drops. Similar to the cell over the coastal plain, this case highlights a process in which the lofting of supercooled water above the melting level, subsequent accretional growth leading to graupel formation, and the melting of the ice hydrometeors contributed to intense rainfall. This convective microphysical scenario, discussed in other studies regarding tropical convection (i.e., MCTEX, Carey and Rutledge 2000; TRMM-LBA, Cifelli et al. 2002), was also conceptually described in the tropical-like convection

of the Fort Collins, Colorado, flood (Petersen et al. 1999) as an "accumulation zone" model of precipitation production through a coupling of warm-rain and ice-particle accretion processes.

3) SMO

Reduced rainfall intensity, frequently observed over the higher terrain of the SMO (relative to lower terrain), has been related to shallower warm-cloud depths compared to the coastal plain (Rowe et al. 2008), as well as to an overall reduced amount of precipitation-sized ice aloft (Nesbitt et al. 2008; Lang et al. 2010). To further investigate these potential differences in microphysical processes, several examples of average, isolated cells over the SMO (>2 km) were selected from 14 August 2004 located, on average, between 90 and 100 km from S-Pol; a day characterized by scattered afternoon convection. Figure 8 shows the presence of graupel as identified by the HID algorithm from three cells on this day. In general, the vertical extent of graupel in these cells was limited to below 10 km, compared to 15 km over the lower elevations. This observation is consistent

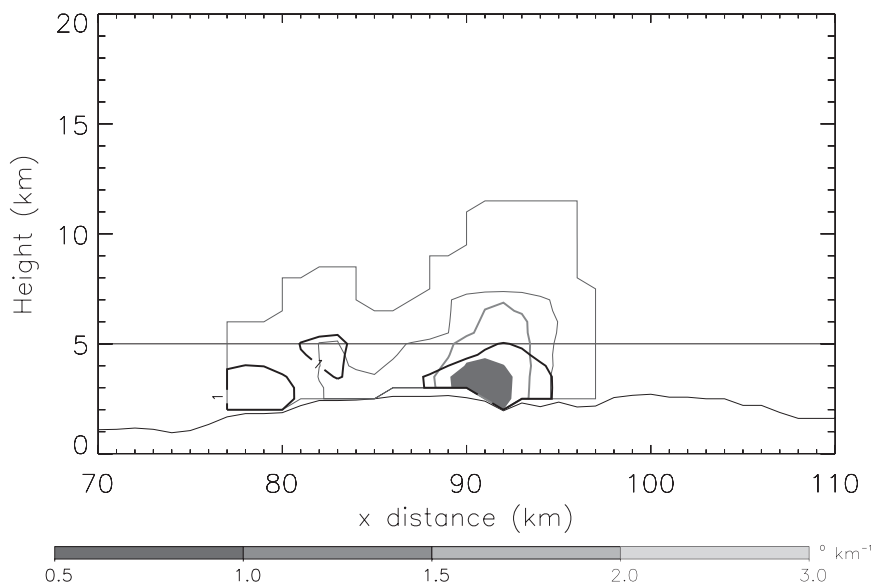


FIG. 9. Vertical cross section through the maximum reflectivity of a cell occurring at 2215 UTC 14 Aug 2004 over the high terrain of the SMO. Filled contours represent K_{DP} ($^{\circ} \text{km}^{-1}$) and the other contours are as in Fig. 4.

with the hypothesis that cells over the higher terrain had a shallower depth of precipitation-sized ice compared to the convection over the coastal plain (Nesbitt et al. 2008).

A vertical cross section through one of these isolated cells over the SMO provides further evidence for reduced warm-cloud depth and overall shallower convection over the high terrain (Fig. 9). Radar echo tops extended to 12 km during this mature stage of the cell, but with a 30-dBZ contour below 8 km, as well as K_{DP} values lower than 1°km^{-1} , possibly due to reduced precipitation water mass below the melting level or to the lack of large drops resulting from less precipitation-sized ice. This cell also lacked a Z_{DR} column; a feature observed in intense cells over lower elevations. The

absence of this characteristic, along with the reduced vertical extent of graupel throughout the cell, suggests lesser emphasis on riming processes in addition to a reduced role of collision-coalescence below the melting level. Reflectivity CFADs for two mature cells on this day (Figs. 10a,b) show increased diagonalization compared to the mature, isolated cell over the western slopes, implying more dominant accretional processes in cells occurring over lower elevations. In addition, the reflectivity mode of 35 dBZ is lower than that over the coastal plain, indicating overall weaker convection. These observations suggest that in addition to the shallower warm-cloud cloud depth in isolated cells over the higher terrain, a reduced dependence on riming in these cells contributed to lower median rainfall rates.

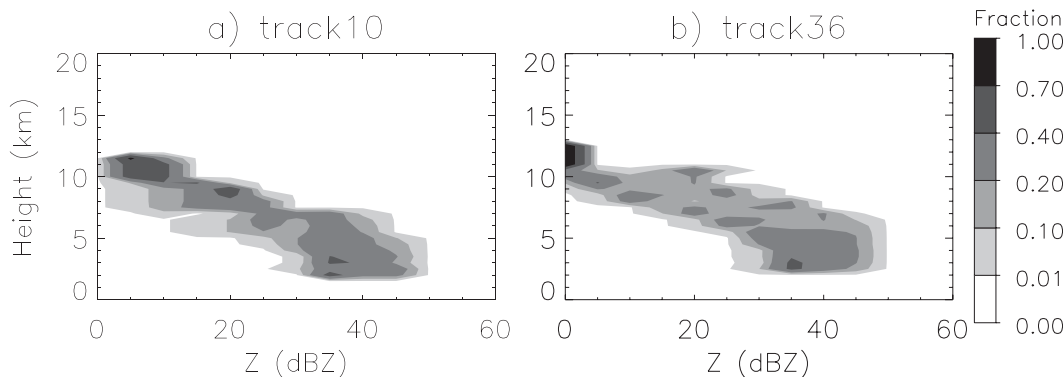


FIG. 10. Reflectivity CFADs for the mature stages of two separate isolated cells on 14 Aug 2004. Frequencies are contoured as in Fig. 7.

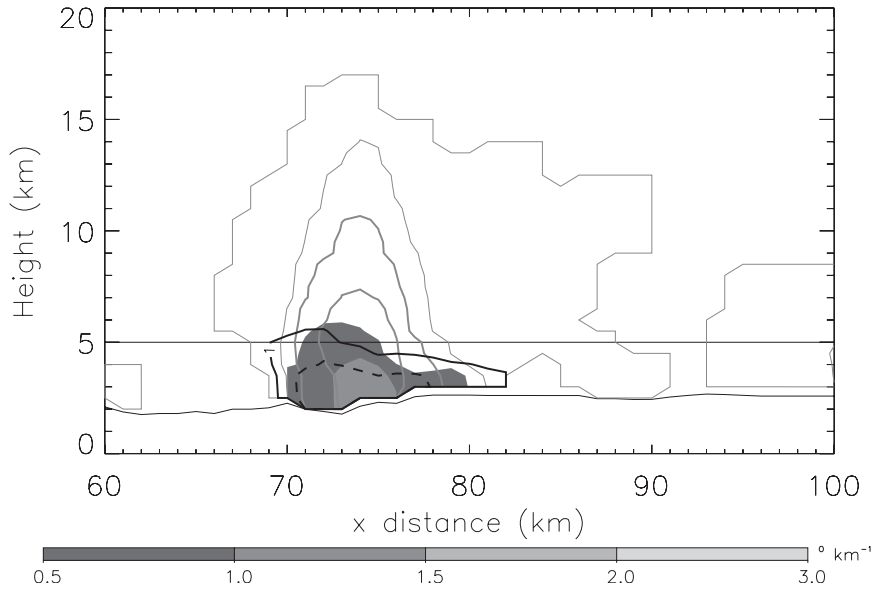


FIG. 11. Vertical cross section through the maximum reflectivity of a cell occurring at 2015 UTC 20 Jul 2004 over the high terrain of the SMO. Filled contours represent K_{DP} ($^{\circ} \text{ km}^{-1}$) and the other contours are as in Fig. 4.

Despite the shallower coalescence zone and reduction in graupel aloft in the examples from 14 August, the potential for higher elevations to receive brief periods of intense rainfall was also prevalent. One particularly intense example occurred around 2015 UTC 20 July 2004, when the cell of interest developed over the higher terrain above 2 km, and gradually moved westward toward the slopes prior to dissipation. A vertical cross section through the cell at this time highlights a deep cell with radar echo extending to 17 km (compared to the median height of 13 km) and the 30-dBZ reflectivity contour approaching 15 km (Fig. 11). The Z_{DR} values greater than 2 dB and K_{DP} exceeding $1^{\circ} \text{ km}^{-1}$ indicate heavy rainfall due to large, oblate hydrometeors;

maximum rainfall rates for this cell were 80 mm h^{-1} , compared to the median of 29 mm h^{-1} for cells over the SMO. The reflectivity CFAD from 2015 UTC (Fig. 12a) shows less diagonalization compared to the previous SMO cases, suggesting a greater role of accretion similar to the lower-elevation examples. Fifteen minutes later (Fig. 12b), however, an increase in diagonalization occurs, beginning with a substantial increase in reflectivity aloft. Similar to the analysis by Zeng et al. (2001), this top-down movement of diagonalization suggests that accretional processes weakened first in the upper levels of the storm where available cloud water was likely depleted more quickly at these colder temperatures compared to lower levels of the cell.

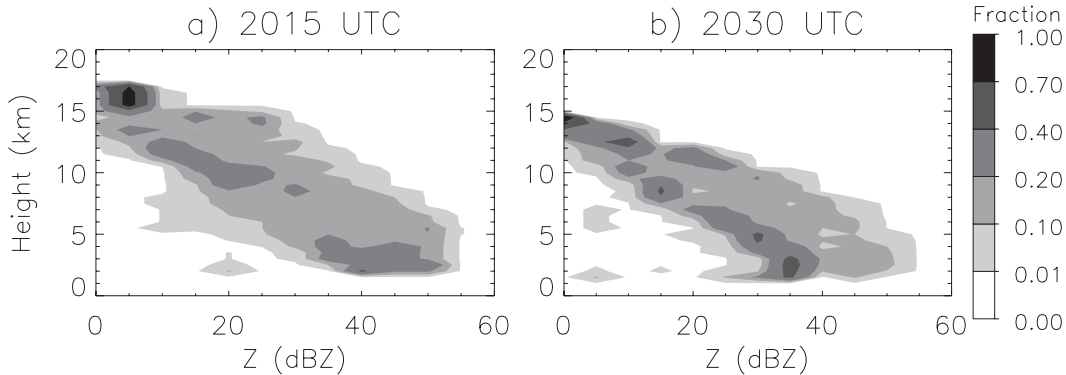


FIG. 12. Reflectivity CFADs for the mature stage of the isolated cell at (a) 2015 and (b) 2030 UTC 20 Jul 2004. Frequencies are contoured as in Fig. 7.

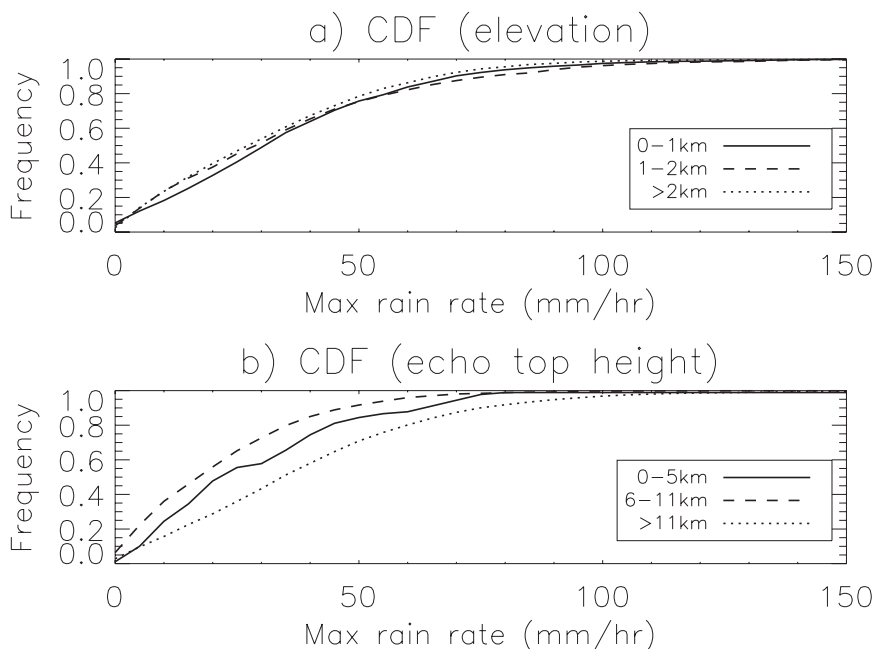


FIG. 13. Cumulative distribution functions of maximum rainfall rate (mm h^{-1}) for all isolated cells partitioned by (a) elevation groups and (b) echo-top height groups.

The only considerable difference between this intense SMO cell and the strong cells described over the lower elevation groups was the reduction in warm-cloud depth. Similar results were described in the Tibetan Plateau region, where convection tended to be maximized upstream of the Himalayas, yet deep convection, with a 40-dBZ echo extending above 10 km, was observed over the high terrain of the plateau despite reduced depth below the melting level (e.g., Houze et al. 2007). This example also coincides with the study by Nesbitt et al. (2008), who also suggested a potentially important role for ice-based microphysical processes over the high terrain.

The examples described above, encompassing a range of topography, highlighted a dependence of mixed-phase microphysical processes in intense cells over all elevations. The previously noted reduction in warm-cloud depth and shallower convection typically discussed in earlier NAME studies of SMO convection is also evident in these examples, leading to a reduced role of collision-coalescence and resultant smaller rainfall rates compared to over the low terrain. However, an intense cell over the high terrain exhibited characteristics similar to those over the coastal plain, with deep cores and polarimetric signatures indicative of large ice hydrometeors above the melting level. To place these intense examples within the larger context of all NAME isolated cells from the microphysical scans, a series of statistics based on the polarimetric radar data were

computed for the elevation groups. These statistics are now described.

b. Average cell characteristics

1) RAINFALL RATE AND ECHO-TOP HEIGHTS

Previous results from NAME (e.g., Gochis et al. 2006, 2007; Lang et al. 2007; Nesbitt et al. 2008; Rowe et al. 2008) emphasized a peak in rainfall intensity along the coastal plain and western slopes of the SMO, hypothesized to be linked to increased warm-cloud depth (Rowe et al. 2008), deeper convection (Nesbitt et al. 2008), and increased ice mass aloft (Lang et al. 2010) over the lower terrain. However, based on comparisons between 24-h and 15-min rainfall totals, Rowe et al. (2008) suggested that rainfall may be intense both over the coast and the higher terrain of the SMO, with a longer duration of heavy precipitation over the lower elevations. The potential for the higher terrain to receive brief periods of intense rainfall was also suggested from rain gauge observations (Gochis et al. 2007) and was observed for one SMO case described in the previous section. Cumulative distribution functions (CDFs) of maximum instantaneous rain rate as a function of maximum terrain height are shown in Fig. 13a for all isolated cells identified in our study. There is a tendency for the most frequent occurrence of intense rainfall rates ($>50 \text{ mm h}^{-1}$) to occur within cells over the slopes (1–2 km), consistent with previous results; however, there is considerably less separation

between elevation groups compared to the distributions that include all precipitating features (i.e., also including mesoscale systems and organized convection) during NAME, shown in Fig. 2 of Rowe et al. (2008). This observation agrees with the hypothesis suggested from the case studies that isolated convection occurring during NAME has the potential to produce brief periods of intense rainfall regardless of the underlying topography.

Previous NAME studies (e.g., Nesbitt et al. 2008; Rowe et al. 2008) have also suggested a relationship between reduced rainfall intensity and lower echo-top heights over the SMO for all precipitating features over the high terrain; however, when considering only isolated convection, selected examples of intense cells, as well as general rainfall statistics (Fig. 13a), showed that intense instantaneous rainfall rates also occurred over the higher elevations. The next step was to relate echo-top heights of each tracked isolated cell to these rainfall statistics and investigate any potential differences, or lack thereof, as a function of topography. First, Fig. 13b shows the CDF of maximum rainfall rates grouped by echo-top height. From this figure, it is evident that the most intense rainfall rates are associated with the deepest convection (i.e., echo-top heights greater than 11 km). The greater rainfall rates associated with shallow convection (0–5 km), compared to cells with echo tops in the range of 6–11 km, reflect the rain-out stage of cells and compose only a small percentage of total cells (<1%).

The presence of deep convection over the SMO, which subsequently produced intense rainfall, was noted in section 3a. To investigate the frequency of occurrence for these intense cells, probability distribution functions of echo-top heights, computed for each tracked cell as the maximum height with Z greater than 0 dBZ, as a function of elevation are displayed in Fig. 14. This plot shows that the most frequent echo-top height observed for isolated cells over the SMO was 11 km, whereas the greatest percentage of low-terrain isolated cells extended to 14 km, suggesting a trend of shallower convection over the higher terrain that is consistent with previous results (e.g., Nesbitt et al. 2008; Rowe et al. 2008). Nesbitt et al. (2008) suggested that echo height over the high terrain is limited by the lack of moisture available at cloud base compared to the lower elevations in proximity to the Gulf of California. However, despite this average tendency for taller echo tops over the low terrain, it is apparent that deep convection can occur over the SMO.

2) POLARIMETRIC OBSERVATIONS

Consistent with the presence of graupel in the examples of convection over both the coastal plain and the SMO (section 3a), results from Nesbitt et al. (2008)

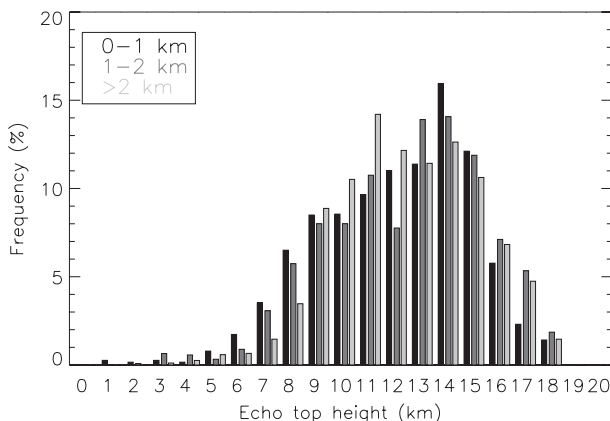


FIG. 14. Histogram of echo-top heights (km), computed for each isolated cell, as a function of terrain height (km). Frequency represents the percentage of cells with the particular echo-top height for the elevation group.

suggested that convection contained significant mixed-phase processes. Petersen et al. (1996) noted a relationship between the extension of the 30-dBZ contour above the melting level and lightning production, providing a minimum condition for the possibility of lightning. However, a number of studies have linked a higher probability of lightning production in cells to the presence of 40-dBZ echo at or above the altitude of -10°C (Laksen and Stansbury 1974; Dye et al. 1989; Buechler and Goodman 1990; Michimoto 1991, 1993; Gremillion and Orville 1999; Vincent et al. 2003). During NAME, the -10°C isotherm typically fell between 6.5 and 7 km; it is therefore assumed that lightning production, and therefore inferred large supercooled and ice water contents, is associated with the extension of the 40-dBZ contour to at least 7 km. The CDF of maximum height of the 40-dBZ contour in cells (Fig. 15) shows that roughly 15% of cells over the lower terrain reach this threshold and more than 20% of cells over the SMO should have a high probability of lightning production. The larger percentage of isolated cells over the SMO with 40 dBZ extending to 7 km compared to over lower elevations is likely a reflection of the greater cloud-base heights over the higher elevations, although the differences between terrain bands are not significantly large. This plot does, however, highlight the likelihood of lightning production over all elevation groups.

Although the mixed-phase processes were inferred for precipitating features over all elevations, Nesbitt et al. (2008) speculated that the generally shallower convection of the SMO produced a smaller depth of precipitation-sized ice particles, which was seen in several examples of average SMO cells in section 3a. In addition to reduced precipitation-ice mass over the

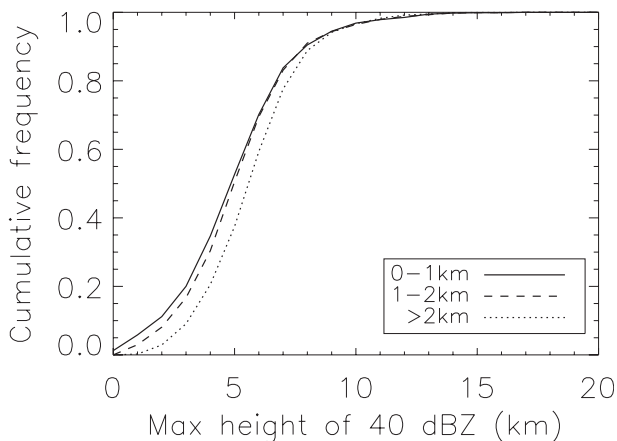


FIG. 15. Cumulative distribution functions of the maximum height of 40-dBZ reflectivity in isolated cells as a function of terrain height (km).

SMO, Lang et al. (2010) also found a reduction in liquid water mass compared to lower terrain for all precipitating features, consistent with the shallower warm-cloud depth over the SMO (Rowe et al. 2008). To investigate differences in the relative amounts of precipitation liquid and precipitation ice for isolated convection during the

microphysical scans, ice and water masses were summed over all grid points within each isolated cell identified and normalized by the volume of the cell. Cumulative distribution functions of these calculations are shown in Figs. 16a,b, which highlight increased ice mass associated with cells over the SMO, and a greater amount of water mass contained in cells over the lower terrain. The increased water mass in cells over lower elevations is consistent with results from Lang et al. (2010) and suggests a greater role of warm-rain processes. The importance of collision-coalescence is also evident in the CDFs of water mass fraction (Fig. 16c), defined as the total precipitation water mass in a cell divided by the total accumulated water and ice mass, which highlights the greater precipitation liquid water fractions over the lower terrain for isolated cells. The reduced amount and depth of rainwater in isolated convection over the SMO likely resulted from smaller warm-cloud depths over the high terrain. Despite this reduced amount of moisture flux at cloud base for cells over the SMO, due to the higher LCL, peak ice mass, which occurred just above the melting level for all elevation groups, was greater compared to cells over lower terrain (Fig. 16d). Previous studies, such as Rosenfeld and Woodley (2003), have noted that a smaller

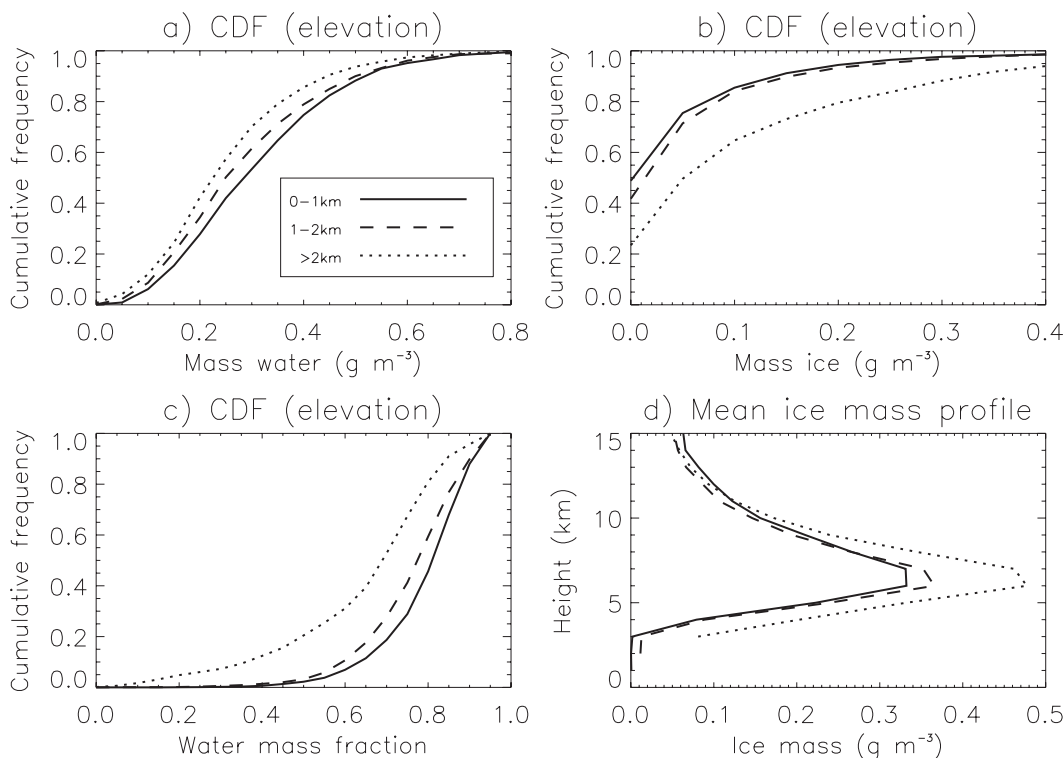


FIG. 16. Cumulative distribution functions as a function of terrain height (km) of (a) water mass, (b) ice mass, (c) water mass fraction, and (d) mean ice mass profile. Water and ice masses (g m^{-3}) are normalized by the total number of points in cells.

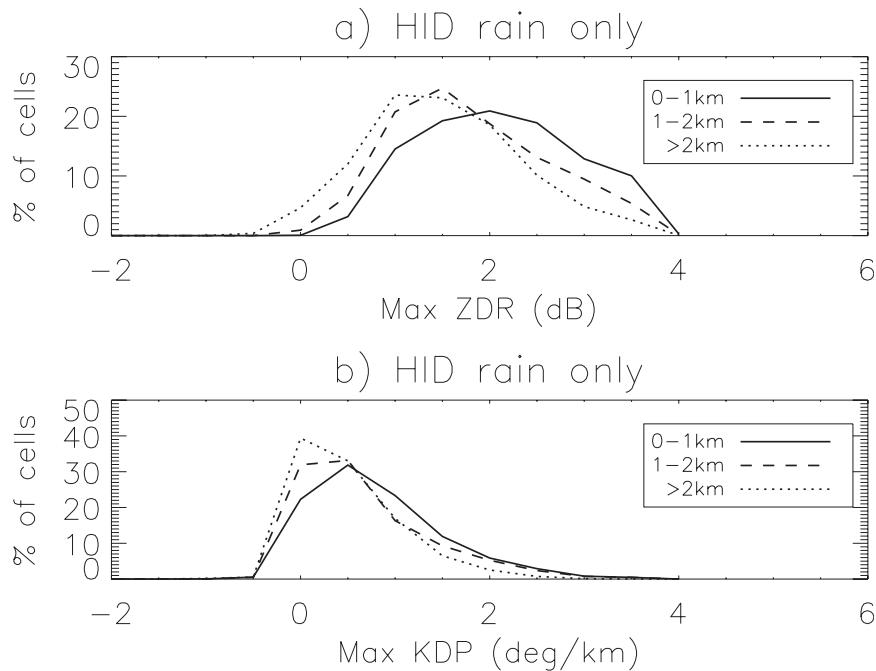


FIG. 17. Probability distribution functions for maximum (a) Z_{DR} (dB) and (b) K_{DP} ($^{\circ} \text{km}^{-1}$) in isolated cells. These plots only include grid points in cells identified by the HID as rain and that occur below the melting level.

warm-cloud depth, implied by a higher cloud-base height, reduces the depth through which warm-rain processes can occur, leaving a greater relative supercooled liquid water available to the mixed phase zone. Therefore, it is likely that the shallower warm-cloud depth in cells over the SMO limited the collision-coalescence process, allowing for a greater percentage of available moisture to be lofted above the melting level, leading to increased ice mass in convection over the higher terrain.

In agreement with these results, Williams et al. (2007), using profiler data, suggested the importance of warm-rain processes at low elevations through evidence of droplet size distribution (DSD) broadening below the melting level. In addition, Lang et al. (2010) noted larger drop sizes over the coastal plain relative to over the SMO. To investigate this further for isolated cells, probability distributions were created of maximum Z_{DR} for portions of cells identified as rain (Fig. 17a). This plot not only shows a tendency for Z_{DR} to be greater in cells over the low terrain, but the distribution is also wider compared to the higher elevations, suggesting a broader DSD and larger drop sizes over the coastal plain that is consistent with the previously described studies. The probability distribution for maximum K_{DP} associated with liquid water in a cell (Fig. 17b) shows a tendency for K_{DP} to be slightly greater over the lower terrain as well, in agreement with greater rainfall rates over these

elevations. This trend likely reflects the larger drop sizes observed over the low terrain (Fig. 17a) due to melting of ice hydrometeors and the increased precipitation water mass due to increased warm-cloud depth associated with these cells (Fig. 16). Both processes would tend to increase K_{DP} .

Contoured frequency diagrams of Z_{DR} and K_{DP} for rain-only points within all isolated cells (Figs. 18a–c) were constructed for each elevation group to further investigate possible differences in precipitation processes. Contoured are the logarithm of normalized frequencies for the elevation group to emphasize the differences in the extremes; normalization here is in regards to total frequency. From these plots, in addition to the high K_{DP} values associated with large Z_{DR} , it is evident that for lower Z_{DR} (between 1 and 2 dB), K_{DP} tends to be slightly higher over the lower elevations. This suggests a significant contribution to K_{DP} , and therefore rain rates, from higher water contents of smaller drops in cells over the low terrain, and further emphasizes the importance of warm-rain processes compared to over the SMO. In addition, case studies in section 3a highlighted the presence of Z_{DR} columns in cells over the low terrain, implying the lofting of liquid water above the melting level, aiding in the growth of large ice hydrometeors. Figure 19 shows a CDF of Z_{DR} for points located above the melting level highlighting a slightly

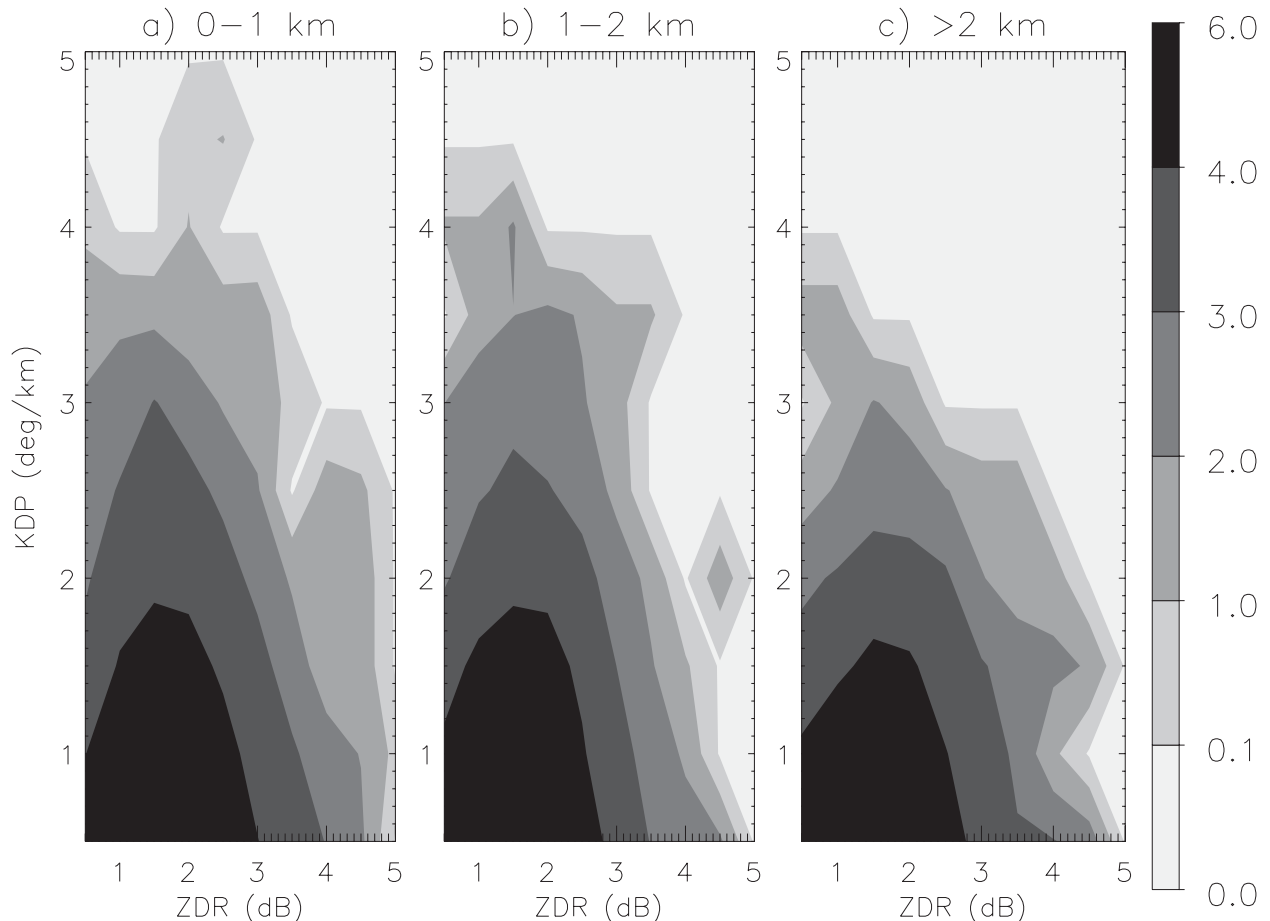


FIG. 18. Contoured frequency diagrams of Z_{DR} (dB) and K_{DP} ($^{\circ} \text{ km}^{-1}$) within portions of isolated cells identified as rain below the melting level. Plotted are the logarithms of frequencies normalized by the total frequency for the elevation group.

greater fraction of positive Z_{DR} at subfreezing temperatures for cells over the low terrain, consistent with the more frequent observations of Z_{DR} columns compared to over the SMO in the case studies. The presence of positive Z_{DR} above the melting level over the SMO, however, is also evident in this plot, suggesting that although less common, isolated convection over the higher terrain produced significant ice mass due to riming, which subsequently melted, producing intense rain rates. This differs from the lower terrain where, in addition to ice-based processes, warm-rain microphysical processes are important for producing copious amounts of rainfall through the addition of higher rain-water contents.

4. Discussion and conclusions

To address the difficulty of predicting warm-season rainfall associated with the North American monsoon, a comprehensive network of instrumentation was deployed

in northwestern Mexico during the summer of 2004. NCAR's S-band polarimetric radar (S-Pol) was used to investigate the location, size, and type of hydrometeors in individual cells during NAME. A cell identification and tracking algorithm was applied to the gridded radar fields during about 100 h of microphysical scans to locate and track individual convective elements meeting prescribed reflectivity and area thresholds. Additional parameters were computed for the tracked cells, including ice and liquid water mass, and near-surface rainfall rates to relate the trends in precipitation intensity to hydrometeor characteristics within the cells. Only isolated cells over land were included for this study to begin to describe the elevation-dependent trends observed in this region.

Cases selected over the entire range of topography revealed deep cells and polarimetric signatures comparable to other studies of tropical (e.g., Carey and Rutledge 2000; Cifelli et al. 2002) and midlatitude convection (e.g., Bringi et al. 1996; Tessendorf et al. 2005). Examples over

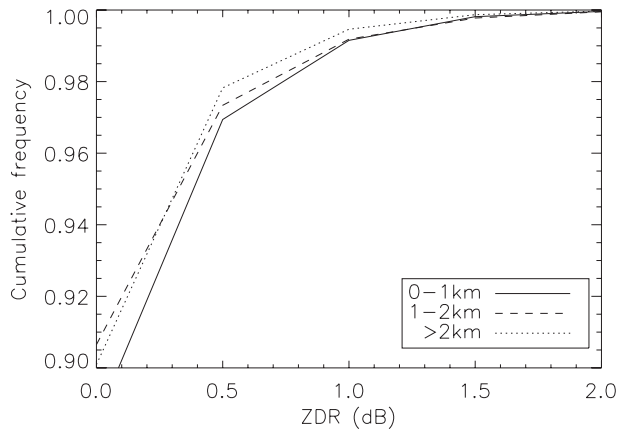


FIG. 19. Cumulative distribution functions for positive Z_{DR} (dB) identified above the melting level in isolated cells.

the coastal plain highlighted deep, isolated convection with precipitation-sized ice extending at times to 15 km. The observance of Z_{DR} columns in these cells indicated the lofting of supercooled water above the melting level, where an enhanced L_{DR} “cap” above the column implied subsequent freezing to produce graupel, which grew rapidly via riming. This process has also been shown to be an important contributor to precipitation-sized ice in tropical convection (e.g., Carey and Rutledge 2000), as well as intense convection observed in the midlatitudes (e.g., Fulton and Heymsfield 1991; Bringi et al. 1997; Zeng et al. 2001; Tessendorf et al. 2005). Contoured frequency by altitude diagrams (CFADs) of reflectivity for isolated cells over the western slopes of the SMO (1–2 km) also suggested a significant contribution from mixed-phase processes, where the observed lack of diagonalization in plots of CFAD reflectivity indicated dominant accretional processes, similar to that observed over the coastal plain. Peaks in Z_H , Z_{DR} , and K_{DP} below the melting level throughout different stages of the cells’ lifetimes highlighted the combined roles of collision–coalescence and melting precipitation-sized ice in these isolated cells, where both warm-rain and ice-based processes were obviously important for producing intense rainfall. In addition, statistics including polarimetric information for isolated cells showed a broader distribution of maximum Z_{DR} in convection over the lower terrain, with a wide range of Z_{DR} also observed for a given K_{DP} value, further indicating the combined roles of large, melting hydrometeors and increased liquid water due to deeper warm-cloud depths, leading to intense rainfall in cells over lower elevations.

A selection of average isolated cells over the SMO on 14 August 2004 showed shallower warm-cloud depths, lower echo-top heights, and a lesser vertical extent of graupel throughout the vertical column, all consistent with previous observations that included all precipitating

features during NAME (e.g., Lang et al. 2007, 2010; Nesbitt et al. 2008; Rowe et al. 2008). The absence of Z_{DR} columns and increased diagonalization for reflectivity frequency distributions in these few examples suggested a reduced contribution from riming processes, in addition to the reduction of collision–coalescence due to shallower warm-cloud depths. Despite the observation of strong upward motion over the SMO, Johnson et al. (2010) noted a lack of a moist column, where the lack of moisture available for latent heat release could likely explain the relative shallowness and reduced dependence on mixed-phase processes for rainfall production at the higher elevations. However, an example shown in section 3a, as well as general statistics including polarimetric information from all isolated cells during the microphysical scans, supported the idea that short-lived, isolated convection over the SMO could produce intense rainfall despite the general tendency for weaker convection compared to over the lower elevations. One such example described an isolated cell that formed over the high terrain near the western slopes, producing heavy rainfall comparable to the low-terrain cases. Melting of large ice hydrometeors was noted, and an increased role of accretion above the melting level was inferred. The general statistics revealed increased ice mass in these particular cells over the SMO just above the melting level, further highlighting an important role of ice in producing intense rainfall during a number of cases over the higher elevations.

These characteristics associated with intense convection over the SMO were similar to convection occurring over the high terrain of the Tibetan Plateau, where despite the tendency for the most intense convective echo to be observed upstream of the Himalayas, deep, intense convection was occasionally observed over the high terrain of the plateau, with truncated lower portions relative to cells over the lower elevations (Houze et al. 2007). The Houze et al. (2007) study also found that in this region, the intense convective echoes organized upscale in some cases to produce vertically erect, intense convective echo embedded within MCSs, which rarely occurred over the plateau. Previous NAME studies (e.g., Lang et al. 2007) also noted the organization of intense convection over the SMO as cells moved toward the western slopes, similar to the Tibetan Plateau region. This process suggests a likely dependence of microphysical processes on degree of organization and will be the focus of a future study to further understand the relative roles of warm-rain and ice-based processes in convection during NAME.

Acknowledgments. We thank those who contributed to the successful deployment of S-Pol during NAME and the subsequent quality control of the data, including Rit

Carbone, Dave Ahijevych, Bob Rilling, Chad Christenson, Lee Nelson, and Gustavo Pereira. Lee Nelson and Dr. Steven Nesbitt are acknowledged for their roles in the development of the cell-tracking algorithm adapted for this study. This research was funded by the National Science Foundation Grant ATM-0733396.

REFERENCES

- Adams, D. K., and A. C. Comrie, 1997: The North American monsoon. *Bull. Amer. Meteor. Soc.*, **78**, 2197–2213.
- Badan-Dangon, A., C. E. Dorman, M. A. Merrifield, and C. D. Winant, 1991: The lower atmosphere over the Gulf of California. *J. Geophys. Res.*, **96**, 877–896.
- Berberly, E. H., 2001: Mesoscale moisture analysis of the North American monsoon. *J. Climate*, **14**, 121–137.
- Bluestein, H. B., and M. H. Jain, 1985: Formation of mesoscale lines of precipitation: Severe squall lines in Oklahoma during the spring. *J. Atmos. Sci.*, **42**, 1711–1732.
- Bringi, V. N., and V. Chandrasekar, 2001: *Polarimetric Doppler Weather Radar Principles and Applications*. Cambridge University Press, 636 pp.
- , L. Liu, P. C. Kennedy, V. Chandrasekar, and S. A. Rutledge, 1996: Dual multiparameter radar observations of intense convective storms: The 24 June 1992 case study. *Meteor. Atmos. Phys.*, **59**, 3–31.
- , K. Knupp, A. Detwiler, L. Liu, I. J. Caylor, and R. A. Black, 1997: Evolution of a Florida thunderstorm during the Convection and Precipitation/Electrification Experiment: The case of 9 August 1991. *Mon. Wea. Rev.*, **125**, 2131–2160.
- Buechler, D. E., and S. J. Goodman, 1990: Echo size and asymmetry: Impact on NEXRAD storm identification. *J. Appl. Meteor.*, **29**, 962–969.
- Carey, L. D., and S. A. Rutledge, 2000: The relationship between precipitation and lightning in tropical island convection: A C-band polarimetric radar study. *Mon. Wea. Rev.*, **128**, 2687–2710.
- Cifelli, R., W. A. Petersen, L. D. Carey, S. A. Rutledge, and M. A. F. Silva-Dias, 2002: Radar observations of the kinematic, microphysical, and precipitation characteristics of two MCSs in TRMM LBA. *J. Geophys. Res.*, **107**, 8077, doi:10.1029/2000JD000264.
- Cotton, W. R., and R. A. Anthes, 1989: *Storm and Cloud Dynamics*. Academic Press, 883 pp.
- Crane, R. K., 1979: Automatic cell detection and tracking. *IEEE Trans. Geosci. Electron.*, **GE-17**, 250–262.
- DeMott, C. A., and S. A. Rutledge, 1998: The vertical structure of TOGA COARE convection. Part I: Radar echo distributions. *J. Atmos. Sci.*, **55**, 2730–2747.
- Dixon, M., and G. Wiener, 1993: TITAN: Thunderstorm Identification, Tracking, Analysis, and Nowcasting—A radar-based methodology. *J. Atmos. Oceanic Technol.*, **10**, 785–797.
- Douglas, M., R. A. Maddox, K. Howard, and S. Reyes, 1993: The Mexican monsoon. *J. Climate*, **6**, 1665–1677.
- Dye, J. E., W. P. Winn, J. J. Jones, and D. W. Breed, 1989: The electrification of New Mexico thunderstorms. 1. Relationship between precipitation development and the onset of electrification. *J. Geophys. Res.*, **94**, 8643–8656.
- Fulton, R., and G. M. Heymsfield, 1991: Microphysical and radiative characteristics of convective clouds during COHMEX. *J. Appl. Meteor.*, **30**, 98–116.
- Gauthier, M. L., W. A. Petersen, and L. D. Carey, 2010: Cell mergers and their impact on cloud-to-ground lightning over the Houston area. *Atmos. Res.*, **96**, 626–632.
- Gochis, D. J., W. J. Shuttleworth, and Z. L. Yang, 2002: Sensitivity of the modeled North American monsoon regional climate to convective parameterization. *Mon. Wea. Rev.*, **130**, 1282–1298.
- , A. Jimenez, C. J. Watts, J. Garatuza-Payan, and W. J. Shuttleworth, 2004: Analysis of 2002 and 2003 warm-season precipitation from the North American Monsoon Experiment event rain gauge network. *Mon. Wea. Rev.*, **132**, 2938–2953.
- , L. Brito-Castillo, and W. J. Shuttleworth, 2006: Hydroclimatology of the North American monsoon region in northwest Mexico. *J. Hydrol.*, **316**, 53–70.
- , C. J. Watts, J. Garatuza-Payan, and J. Cesar-Rodriguez, 2007: Spatial and temporal patterns of precipitation intensity as observed by the NAME event rain gauge network from 2002 to 2004. *J. Climate*, **20**, 1734–1750.
- Gremillion, M. S., and R. E. Orville, 1999: Thunderstorm characteristics of cloud-to-ground at the Kennedy Space Center, Florida: A study of lightning initiation signatures as indicated by the WSR-88D. *Wea. Forecasting*, **14**, 640–649.
- Higgins, R. W., Y. Yao, and X. L. Wang, 1997: Influence of the North American monsoon system on the U.S. summer precipitation regime. *J. Climate*, **10**, 2600–2622.
- , and Coauthors, 2006: The NAME 2004 field campaign and modeling strategy. *Bull. Amer. Meteor. Soc.*, **87**, 79–94.
- Houze, R. A., Jr., D. C. Wilton, and B. F. Smull, 2007: Monsoon convection in the Himalayan region as seen by the TRMM precipitation radar. *Quart. J. Roy. Meteor. Soc.*, **133**, 1389–1411.
- Hubbert, J., and V. N. Bringi, 1995: An iterative filtering technique for the analysis of copolar differential phase and dual-frequency radar measurements. *J. Atmos. Oceanic Technol.*, **12**, 643–648.
- Illingworth, A. J., J. W. F. Goddard, and S. M. Cherry, 1987: Polarization radar studies of precipitation development in convective storms. *Quart. J. Roy. Meteor. Soc.*, **113**, 469–489.
- Jameson, A., 1983: Microphysical interpretation of multi-parameter radar measurements in rain. Part I: Interpretation of polarization measurements and estimation of raindrop shapes. *J. Atmos. Sci.*, **40**, 1792–1802.
- , M. Murphy, and E. Krider, 1996: Multiple-parameter radar observations of isolated Florida thunderstorms during the onset of electrification. *J. Appl. Meteor.*, **35**, 343–354.
- Johnson, J. T., P. L. MacKeen, A. Witt, E. D. Mitchell, G. J. Stumpf, M. D. Eilts, and K. W. Thomas, 1998: The storm cell identification and tracking algorithm: An enhanced WSR-88D algorithm. *Wea. Forecasting*, **13**, 263–276.
- Johnson, R. H., P. E. Cielsielski, T. S. L'Ecuyer, and A. J. Newman, 2010: Diurnal cycle of convection during the 2004 North American Monsoon Experiment. *J. Climate*, **23**, 1060–1078.
- Keenan, T., and Coauthors, 2000: The Maritime Continent Thunderstorm Experiment (MCTEX): Overview and some results. *Bull. Amer. Meteor. Soc.*, **81**, 2433–2455.
- Laksen, H. R., and E. J. Stansbury, 1974: Association of lightning flashes with precipitation cores extending to height 7 km. *J. Atmos. Terr. Phys.*, **36**, 1547–1553.
- Lang, T. J., D. A. Ahijevych, S. W. Nesbitt, R. E. Carbone, S. A. Rutledge, and R. Cifelli, 2007: Radar-observed characteristics of precipitating systems during NAME 2004. *J. Climate*, **20**, 1713–1733.

- , S. W. Nesbitt, and L. D. Carey, 2009: On the correction of partial beam blockage in polarimetric radar data. *J. Atmos. Oceanic Technol.*, **26**, 943–957.
- , S. A. Rutledge, and R. Cifelli, 2010: Polarimetric radar observations of convection in northwestern Mexico during the North American Monsoon Experiment. *J. Hydrometeor.*, **11**, 1345–1357.
- Li, L., W. Schmid, and J. Joss, 1995: Nowcasting of motion and growth of precipitation with radar over a complex orography. *J. Appl. Meteor.*, **34**, 1286–1300.
- Liu, H., and V. Chandrasekar, 2000: Classification of hydrometeors based on polarimetric radar measurements: Development of fuzzy logic and neuro-fuzzy systems, and in situ verification. *J. Atmos. Oceanic Technol.*, **17**, 140–164.
- Michimoto, K., 1991: A study of radar echoes and their relation to lightning discharge of thunderclouds in the Hokuriku District. Part I: Observation and analysis of thunderclouds in summer and winter. *J. Meteor. Soc. Japan*, **69**, 327–335.
- , 1993: A study of radar echoes and their relation to lightning discharge of thunderclouds in the Hokuriku District. Part II: Observation and analysis of “single flash” thunderclouds in midwinter. *J. Meteor. Soc. Japan*, **71**, 195–204.
- Mohr, C. G., L. Jay Miller, R. L. Vaughan, and H. W. Frank, 1986: The merger of mesoscale datasets into a common Cartesian format for efficient and systematic analyses. *J. Atmos. Oceanic Technol.*, **3**, 143–161.
- Nesbitt, S. W., R. Cifelli, and S. A. Rutledge, 2006: Storm morphology and rainfall characteristics of TRMM precipitation features. *Mon. Wea. Rev.*, **134**, 2702–2721.
- , D. J. Gochis, and T. J. Lang, 2008: The diurnal cycle of clouds and precipitation along the Sierra Madre Occidental observed during NAME-2004: Implications for warm season precipitation estimation in complex terrain. *J. Hydrometeor.*, **9**, 728–743.
- Pereira, L. G., 2008: Characteristics and organization of precipitating features during NAME 2004 and their relationship to environmental conditions. Ph.D. dissertation, Atmospheric Science, Colorado State University, Fort Collins, CO, 229 pp.
- Petersen, W. A., S. A. Rutledge, and R. E. Orville, 1996: Cloud-to-ground lightning observations from TOGA COARE: Selected results and lightning location algorithms. *Mon. Wea. Rev.*, **124**, 602–620.
- , and Coauthors, 1999: Mesoscale and radar observations of the Fort Collins flash flood of 28 July 1997. *Bull. Amer. Meteor. Soc.*, **80**, 191–216.
- Rickenbach, T. M., and S. A. Rutledge, 1998: Convection in TOGA COARE: Horizontal scale, morphology, and rainfall production. *J. Atmos. Sci.*, **55**, 2715–2729.
- Rinehart, R. E., and E. T. Garvey, 1978: Three-dimensional storm motion detection by conventional weather radar. *Nature*, **273**, 287–289.
- Rosenfeld, D., 1987: Objective method for analysis and tracking of convective cells as seen by radar. *J. Atmos. Oceanic Technol.*, **4**, 422–434.
- , and W. L. Woodley, 2003: Closing the 5-year circle: From cloud seeding to space and back to climate change through precipitation physics. *Cloud Systems, Hurricanes, and the Tropical Rainfall Measuring Mission (TRMM)*, Meteor. Monogr., No. 51, Amer. Meteor. Soc., 59–80.
- Rowe, A. K., S. A. Rutledge, T. J. Lang, P. E. Ciesielski, and S. M. Saleeby, 2008: Elevation-dependent trends in precipitation observed during NAME. *Mon. Wea. Rev.*, **136**, 4962–4979.
- Takahashi, T., 1990: Near absence of lightning in torrential rainfall producing Micronesian thunderstorms. *Geophys. Res. Lett.*, **17**, 2381–2384.
- , and K. Kuhara, 1993: Precipitation mechanisms of cumulonimbus clouds at Pohnpei, Micronesia. *J. Meteor. Soc. Japan*, **71**, 21–31.
- Tessendorf, S. A., L. J. Miller, K. C. Wiens, and S. A. Rutledge, 2005: The 29 June 2000 supercell observed during STEPS. Part I: Kinematics and microphysics. *J. Atmos. Sci.*, **62**, 4127–4150.
- Vincent, B. R., L. D. Carey, D. Schneider, K. Keeter, and R. Gonski, 2003: Using WSR-88D reflectivity data for the prediction of cloud-to-ground lightning: A North Carolina study. *Natl. Wea. Dig.*, **27**, 35–44.
- Williams, C. R., A. B. White, K. S. Gage, and F. M. Ralph, 2007: Vertical structure of precipitation and related microphysics observed by NOAA profilers and TRMM during NAME 2004. *J. Climate*, **20**, 1693–1712.
- Yuter, S. E., and R. A. Houze, 1995: Three-dimensional kinematic and microphysical evolution of Florida cumulonimbus. Part II: Frequency distributions of vertical velocity, reflectivity, and differential reflectivity. *Mon. Wea. Rev.*, **123**, 1941–1963.
- Zeng, Z., S. E. Yuter, R. A. Houze Jr., and D. E. Kingsmill, 2001: Microphysics of the rapid development of heavy convective precipitation. *Mon. Wea. Rev.*, **129**, 1882–1904.